IMECE2005-81503

TAILORED NANOSCALE CONTRAST AGENTS FOR MAGNETIC RESONANCE IMAGING

Alex J. Barker
University of Colorado, Boulder
Department of Mechanical Engineering
427 UCB, Boulder, CO 80302
Alexander.Barker@Colorado.edu

Brant Cage
National Institute of Standards and
Technology
Boulder, CO, 80305
bcage@boulder.nist.gov

Stephen Russek
National Institute of Standards and
Technology
Boulder, CO, 80305
russek@boulder.nist.gov

Ruchira Garg
The Children's Hospital
Cardiology Division
Denver, CO, 80218
Garg.Ruchira@tchden.org

Robin Shandas
The Children's Hospital
Cardiology Division
Denver, CO, 80218
Shandas.Robin@tchden.org

Conrad R. Stoldt
University of Colorado, Boulder
Department of Mechanical Engineering
427 UCB, Boulder, CO 80302
Conrad.Stoldt@colorado.edu

ABSTRACT

Two potential molecular imaging vectors are investigated for material properties and magnetic resonance imaging (MRI) contrast improvement. Monodisperse magnetite (Fe_3O_4) nanocrystals ranging in size from 7 to 22 nm are solvothermally synthesized by thermolysis of Fe(III) acetylacetonate ($Fe(AcAc)_3$) both with and without the use of heptanoic acid (HA) as a capping ligand. For the resulting Fe_3O_4 nanocrystals, X-Ray diffraction (XRD), transmission electron microscopy (TEM), high-resolution TEM (HRTEM), and superconducting quantum interference device magnetometry (SQUID) is used to identify the average particle size, monodispersity, crystal symmetry, and magnetic properties of the ensembles as a function of time. The characterization study indicates that the HA synthesis route at 3 hours produced nanoparticles with the greatest magnetic anisotropy (15.8×10^4 J/m^3). The feasibility of Fe_8 single molecule magnets (SMMs) as a potential MRI contrast agent is also examined. SQUID magnetization measurements are used to determine anisotropy and saturation of the potential agents. The effectiveness of the Fe_3O_4 nanocrystals and Fe_8 as potential MRI molecular probes is evaluated by MRI contrast improvement using 1.5 mL phantoms dispersed in de-ionized water. Results indicate that the magnetically optimized Fe_3O_4 nanocrystals and Fe_8 SMMs hold promise for use as contrast agents based on the reported MRI images and solution phase T_1/T_2 shortening.

INTRODUCTION

The progression of research in the past decade regarding cellular pathophysiology and the expression of molecular markers has made the concept of molecular contrast imaging an exciting possibility [1]. For example, with traditional MRI imaging, abnormalities indicating disease are usually identified only after careful examination of grayscale computer images by highly trained physicians. The difference between the image contrast of abnormal and normal tissue is often the only non-invasive method available for disease diagnosis. Thus, clinical assessment is challenging, requiring a great deal of subjectivity, skill, and past experience. In addition, the identification of a pathological process can't occur without the abnormal tissue reaching some detection level limited by the imaging tool resolution. This, unfortunately means that the diseased tissue can't be detected immediately; rather, detection is prolonged until a critical detection size is reached [1].

With this in mind, targeted contrast agents possessing the ability to bind and amplify the signature of disease specific molecules promises to improve disease detection beyond the current resolution of traditional imaging. In particular, targeted magnetic nanoparticles may provide a significant improvement in diagnostic MRI. Applications involving paramagnetic nanoparticles (~ 250 nm) have already been successfully implemented for improved MRI imaging of thrombus formation in dogs, plaque formation in rabbits, and drug delivery *in vitro* [2-4]. Thus, this body of work attempts to build on these experiments by optimizing and evaluating the magnetic material properties of an ensemble of Fe_3O_4 monodisperse iron oxide nanoparticles (MIONs) and the single molecule magnet (SMM) known as Fe_8 – both vectors capable of target specific bioconjugation. This paper summarizes our earlier work examining the thermomagnetic properties of Fe_3O_4 and Fe_8 [5, 6] in addition to the evaluating the two vectors for effectiveness as T1/T2 shortening agents.
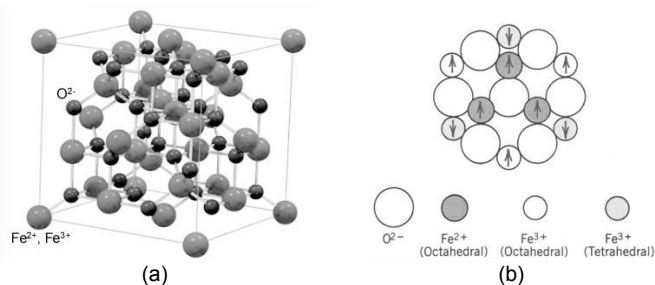
Fig. 1: (a) Fe_3O_4 bulk lattice. (b) Simplified schematic showing the spin moment configurations for Fe^{3+} and Fe^{2+} ions in Fe_3O_4 [7].

Fig. 2: Chemical and magnetic spin moment configuration of Fe_8 [6, 14, 15].

Compared to low-molecular weight water soluble gadolinium chelates (such as Gd-DPTA), the relatively large size of MIONs (after the ~20 nm magnetic core is functionalized with a biodegradable coating) means that iron oxide agents typically do not leak into the interstitium. Therefore, these agents act as intravascular contrast agents or blood pool agents as long the vessel endothelium is not altered by pathological processes [8]. We also consider the potential use of the smaller (~1.5nm) iron based SMM $[Fe_8O_2(OH)_{12}(1,4,7\text{-triazacyclononane})_6]Br_8 \cdot 9H_2O$, or Fe_8 for use in extravascular applications. Thus, we consider two agents for intravascular and extravascular use, both of which are superparamagnetic.

Fe_3O_4, or more specifically $Fe^{2+}O^{2-}\text{-}(Fe^{3+})_2(O^2)_3$, forms an inverse spinel crystal structure in which the cations exist in both +2 and +3 valence states with the ratio of 1:2 [7]. The bulk lattice consists of magnetically neutral O^{2-} anions and Fe^{3+} and Fe^{2+} cations [9] as shown in Fig. 1a with a measured cubic unit cell 0.8 nm [10]. The Fe^{3+} cations exist in both the octahedral and tetrahedral sites in equal numbers, aligned anti-parallel to each other, thus canceling their contribution to the net magnetic moment. Therefore, magnetite derives its net magnetic moment from the parallel spins of the octahedral Fe^{2+} atoms shown in the idealized two-dimensional schematic in Fig. 1b. Thus, a 10 nm iron oxide particle contains several thousand paramagnetic Fe ions, and if the Fe ions are magnetically ordered within the crystal, the net magnetic moment of the nanoparticle can greatly exceed individual molecules of paramagnetic ions [8].

One of the best known and extensively studied SMMs is Fe_8 [11], whose structure is shown in Fig. 2. At low temperatures the spin arrangement can be thought of that as shown by the arrows in Fig. 2 [12], where six Fe^{3+} are aligned antiparallel to two Fe^{3+}, resulting in an overall electronic spin S=10. At room temperature the magnetic structure is less well known and will be more complex than an S=10 macrospin. However, the attractive qualities of Fe_8 for our investigation are aqueous solubility, possible ligand modification for bioconjugation, the large moment per molecule, and homogenous identical molecules [6]. The size of these individual Fe_8 molecular units, allows for the potential to navigate leaky tight junctions present in pathogenic angiogenesis [13].

One commonly employed preparation method for high quality magnetic nanoparticles is the solvo-thermal synthesis route, where nanoparticles are nucleated and grown at elevated temperatures (150-300°C) in a high-boiling point solvent from

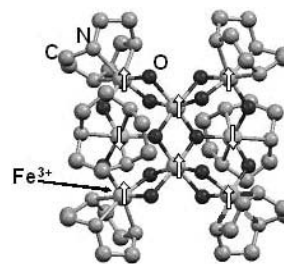one or more organo-metallic precursors [16, 17, 22-24]. Critical to controlling the physical properties of nanoparticles grown by this route are the choice of solvent and the inclusion of a stabilizing agent [23, 25]. While the solvent provides a medium for particle nucleation and growth from diffusing monomers, the stabilizing agent acts to mediate particle growth through chemical interaction with the particle's surface. In general, the processes involved with nanoparticle nucleation and growth in hot solvent are not completely understood and as a consequence, the ability to synthetically prescribe key material properties remains an experimental challenge.

For the Fe_3O_4 ensembles, the size, dispersity and crystal structure of the nanoparticles are critical factors that influence the bulk magnetic properties [16-20]. For example, the transition of a magnetic particle from the single to multi-domain state is dictated by the composition, size, and shape of the particle [21]. Furthermore, the monodispersity and crystal structure of the particle ensemble are crucial in determining the blocking temperature, saturation magnetization, and coercivity of the magnetic system [17-19, 22]. Considering the recent observation of an oriented attachment mechanism in the ripening regime of ceramic nanocrystal growth [26, 27], the presence of this and other defect causing equilibration processes can significantly impact the material properties of the particle ensemble during ripening. For example, ripening based degradation of magnetic properties can occur due to interfacial defects such as grain boundaries and twinned planes common in coalescence and oriented attachment type growth [20, 28, 29].

In the first phase of this work, we identify and control the negative effects of ripening-based growth on nanocrystal structure and material properties by adding an additional stabilizing agent to the synthetic protocol [5]. The magnetite (Fe_3O_4) nanoparticles are synthesized by solvo-thermal processing from a single organo-metallic precursor in a high-boiling point solvent. The Fe_3O_4 surface is an electron pair donor, or a Lewis base [30], while the solvent used in these studies is a weak Lewis acid. As a consequence, the solvent only passively interacts with the Fe_3O_4 surface during growth. The added stabilizing agent, on the other hand, is a strong Lewis acid that demonstrates a high affinity for the nanoparticle [31], and therefore acts to mediate the growth processes in solution. Smoluchowski, Ostwald ripening, and oriented attachment are present in both Fe_3O_4 producing reactions. However, the degree to which these mechanisms are active determines the amount of undesired crystalline defects (thereby determining the end magnetic properties). Thus, we show the addition of an appropriate stabilizing agent not only slows the overall growth rate, but also preserves single crystal structure

and properties through the inhibition of nanoparticle coalescence during equilibration [5]. As a result, the improved magnetic anisotropy of each tailored particle should have a larger effect on the T_2 and T_2^* relaxation times during MRI sequencing [8].

In the second phase of our work, we continue previous work [6] by observing contrast improvement in MRI phantoms containing our optimized Fe_3O_4 samples and Fe_8 SMMs in deionized (DI) water using T_1 and T_2 weighted imaging.

EXPERIMENTAL SECTION

A. Materials

Trioctylamine (98%), Fe(III)-acetylacetonate (further referred to as Fe(Acac)$_3$, 97%), heptanoic acid (99%), anhydrous toluene (99.8%), and ethanol were purchased from Aldrich. All chemicals were used as purchased from the manufacturer and no further purification steps were taken.

B. Synthesis of Fe_3O_4 Nanocrystallites

Fe_3O_4 nanocrystallites were synthesized in the absence of a secondary stabilizing agent by heating 20 mL of trioctylamine to reflux (260°C) under nitrogen gas in a three necked round bottom flask. The solution was mixed using a magnetic stir bar. Upon reaching temperature, 0.045 M Fe(Acac)$_3$ was carefully added to the solvent. The solution immediately turned a dark opaque brown. 1.5 mL aliquots were taken from the solution at 1, 3, 6, and 24 hours. The experiment was halted at 72 hours by quenching the solution with toluene. The resulting product was a clear brown solvent with a black precipitate. The precipitate proceeded to agglomerate in the area surrounding the magnetic stir bar after mixing was halted.

A second experiment, similar to the first, included heptanoic acid (HA) acting as an additional stabilizing agent. For this protocol, a 20% molar concentration of heptanoic acid was added to the trioctylamine. Here, 18.6 mL trioctylamine and 1.4 mL heptanoic acid were heated to reflux (260°C) according to the process described previously. 0.045 M Fe(Acac)$_3$ was carefully added to the solvent and the solution immediately turned a translucent reddish-brown color. 1.5 mL aliquots were taken from the solution at 1, 3, 6, and 24 hours. The experiment was quenched with toluene after 72 hours. The aliquot at 1 hour yielded no precipitate and only the bright red solution was visible. For aliquots that did have a precipitate, the solvent was a clear red-brown with a black precipitate. The precipitate agglomerated around the stir bar after the experiment was terminated.

All of the aliquots along with the final product from the two experiments were centrifuged at 4000 RPM for 15 minutes and washed three times in toluene to remove the excess organic material (Allegra X-22, SX4250 Rotor, Beckman Coulter). Precipitate obtained after centrifugation was resuspended in toluene and labeled TOA for the trioctylamine-only system, and HA/TOA for the heptanoic acid/trioctylamine system. In the case of samples that yielded no precipitate, the samples were kept in solution and no further steps were taken to obtain a precipitate.

C. Synthesis of Fe_8 SMMs

The Fe_8 molecular magnets were synthesized by methods outlined in literature [11] and stored as a refrigerated crystal until used for SQUID magnetometry and the MRI contrast evaluation.

D. Characterization of Materials

Powder X-ray diffraction (XRD), transmission electron microscopy (TEM), and high-resolution TEM (HRTEM) were performed on the Fe_3O_4 aliquots and final product to determine product size, the particle size distribution (PSD), and crystal structure. Powder XRD measurements were obtained using a Scintag Pad V diffractometer equipped with a Cu K radiation source (λ=1.540562 nm). Samples were scanned from $2\theta = 15$ to $2\theta = 90$ at a scan rate of 2 deg./min. TEM micrographs were obtained on a Philips CM10 operating at 80 kV. Over 1000 Fe_3O_4 particles were counted from TEM micrographs taken at different areas on the carbon-coated grid to obtain each aliquot's PSD. HRTEM micrographs and tilt series experiments were performed on a FEI Tecnai TF20 electron microscope with an accelerating voltage of 200kV. All TEM samples were prepared by placing a drop of the nanoparticle-containing solution on clean weighing paper and placing the grid on top of the drop.

For two representative Fe_3O_4 samples consisting of particles synthesized after 3 hours in the HA/TOA and TOA-only system, a commercial SQUID magnetometer (Quantum Design, MPMS-7) was used to perform magnetic measurements as a function of applied field and temperature. Zero-field cooled (ZFC), field cooled (FC), and field sweep measurements were then obtained for each sample. The ZFC and FC measurements were obtained at a field strength, H = .01 T and the field sweep was obtained over the range of -1 T ≤ H ≤ 1 T at 300 K. Field sweep measurements of Fe_8 in a solution of DI water and as a powder were performed over the range of -7 T ≤ H ≤ 7 T at room temperature to observe possible saturation.

E. MRI Phantom Imaging

Magnetic resonance images of the contrast agents were obtained with a Magnetom Avanto (Siemens Medical Solutions, Malvern, PA). Contrast agents were mixed with deionized (DI) water and loaded into 1.5 ml Eppendorf tubes. Each sample tube was loaded upright in the circularly polarized extremity coil surrounded by air. The solutions were imaged by use of routine sequences for magnetic resonance angiography. A control was also prepared consisting only of DI water. All Gradient spin images had the following parameters: image matrix 256 x 256, pixel spacing 0.59 mm x 0.59 mm, imaging frequency 63.67 MHz, magnetic field strength of 1.5 T, and averaged twice.

The Fe_3O_4 10 nm and 24 nm nanoparticle concentration was 1.9 μM (0.005 g Fe_3O_4 / L) which is similar to the concentration used by Ruehm [3] for nanoparticles. For all Fe_3O_4 images the flip angle was 10 degrees. T_1 weighted images had a time to repetition (TR) of 0.012 s and a time to echo (TE) of 0.005 s. T_2 weighted images had a TR of 5.210 s and a TE of 0.096 s.

The Fe8 concentration was 0.0046 M (0.257 g Fe / L), which is similar in order to the recommended concentration of Feridex® (Berlex Laboratories, NJ) for *in-vivo* use. For all Fe_8 images the flip angle was 25 degrees,. For the T_1 weighted images the TR was 0.400 s and the TE was 0.015 s for a single
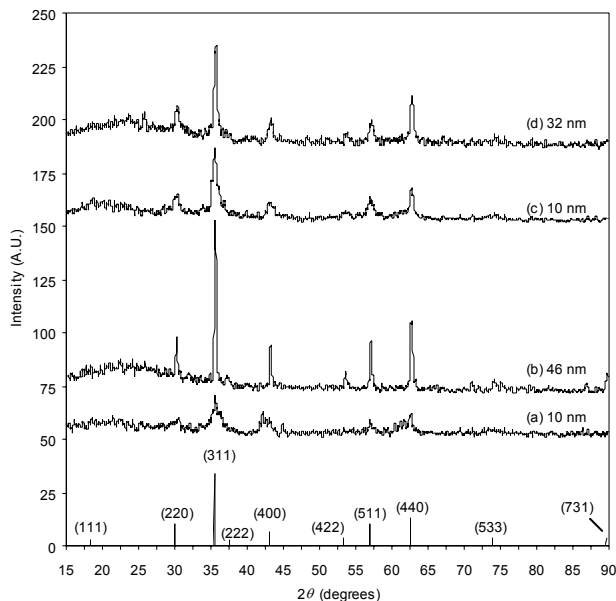
Fig. 3: XRD patterns for magnetite nanocrystallites precipitated in TOA at (a) 3 hrs, (b) 72 hrs, and in HA/TOA at (c) 3 hrs and (d) 72 hrs reaction time. Average crystallite sizes as calculated by Scherrer broadening are shown for each respective pattern. The magnetite reference spectrum is shown at the bottom of the graph for comparison [5].

average. For the T_2 weighted images the TR was 5.070 s and the TE was 0.113 s [6].

RESULTS AND DISCUSSION

In our single precursor solvo-thermal process, the thermal decomposition of Fe(Acac)$_3$ at 260°C provides the source of iron and oxygen monomers for growth of the Fe$_3$O$_4$ nucleate phase in TOA. During growth, the presence of coordinating molecules such as TOA and HA mediate monomer incorporation and stabilize growing particles, as well as prevent particle aggregation due to Van der Waals and magnetic attractive forces [32]. The coordinating molecules preferentially adsorb on the surface of Fe$_3$O$_4$ nucleates, effectively 'capping' the inorganic phase with an organic monolayer. As a result, monomer incorporation and coarsening effects such as Ostwald ripening are either mitigated or slowed [32, 33]. However, by way of a simple Lewis acid/base analysis, HA (the more acidic of the two coordinating molecules) will have a stronger affinity for the more basic iron oxide surface [30, 31]. In principle, and as shown in this work, the presence of HA on the surface of the particle slows both growth by diffusion and coarsening of the particle to a significantly greater degree than a TOA-only reaction. It should be noted that in preliminary experiments not reported here, the use of biphenyl ether as a non-coordinating solvent yielded very large (approximately 200-400 nm in diameter) nanoparticle aggregates due to unrestrained coalescence during ripening.

In Fig. 3, the resulting XRD patterns from the two experiments (TOA-only and HA/TOA) are shown for reaction times of 3 and 72 hours. Scherrer broadening calculations at the (311), (511), and (440) peaks give the average crystallite size for the aliquots as a function of time (without considering

contributions from crystal stress). TEM images are used to confirm the crystallite sizes obtained by the Scherrer analysis. In general, a close agreement between particles sizes estimated from XRD and TEM data indicates that the majority of the synthesized particles are single crystalline. However, some discrepancies between the two measurements are found in this work, the cause of which is attributed to unrestrained nanoparticle coalescence during equilibration. As seen in Fig. 3, both the TOA-only and HA/TOA reactions primarily yield Fe$_3$O$_4$ crystallites at 260°C. In both cases, a reaction time of 3 hours gives an average particle size of 10 nm. After a reaction time of 72 hours, the average particles sizes for each experiment are seen to diverge, with the TOA-only protocol producing a larger average particle diameter with time.

TEM images and their respective PSD's are shown in Fig. 4 for nanoparticles grown by the TOA-only reaction protocol at 260°C. When the TOA-only system is examined, the weaker coordination of TOA to the iron oxide surface yields a higher growth rate compared to the data shown for the HA/TOA system. At 1 hour, the majority of the particles grown in TOA-only have an average diameter near 8 nm, with a smaller population of larger particles (Fig. 4 a-b). After 3 hours, the PSD is bimodal with a majority of the particles having an average diameter near 26 nm. As with the larger particles in Fig. 4a, the particles grown for 3 hours appear irregular in shape with very coarse edges. After 24 hours, the particles grown in the TOA-only reaction become less irregular in shape than at earlier times, but show a significantly broader PSD (Fig. 4 e-f) with diameters as large as 104 nm.

TEM images and their respective PSD's are shown in Fig. 5 for nanoparticles grown by the HA/TOA protocol at 260°C. Particles grown for 1 hour in HA/TOA appear regular in shape with relatively smooth edges, and possess a narrow PSD with an average diameter near 6 nm (Fig. 5 a-b). After 3 hours, the particles remain regular in shape with smooth edges, and show a focused PSD with an average diameter near 10 nm (Fig. 5 c-d). After 24 hours, the particles grown in the HA/TOA system maintain a regular, compact shape with smooth edges (Fig. 5 e-f). Furthermore, the PSD remains narrow when compared to the particles grown in the TOA-only reaction. From these results, it is evident that the addition of HA to the reaction acts to slow the overall nanoparticle growth process. This confirms our notion that growth rates are faster in the system with a lower affinity stabilizing agent.

The average crystallite size of the TOA synthesized particles as determined from the XRD spectrum (Fig. 3a) is only 10 nm, while the TEM and PSD data shown in Fig. 4 c-d indicate an average particle diameter of near 22 nm. We determined that this discrepancy in the estimated size is caused by polycrystalline structure in the TOA-only particles. This conclusion is confirmed through the analysis and comparison of a HRTEM tilt series collected for the TOA-only and HA/TOA nanoparticles. The HRTEM tilt series for the TOA-only nanoparticles is shown in the upper panel of Fig. 6. The series displays irregular contrasts within the particle volume boundary during rotation, showing asymmetry within the crystal structure and confirming that the particles are indeed polycrystalline (representative particles are labeled a-c) [29]. In contrast, the tilt series shown for the HA/TOA system in Fig. 6 displays a highly regular particle crystal structure with no asymmetric contrast within the individual particles (d-f). This observation is
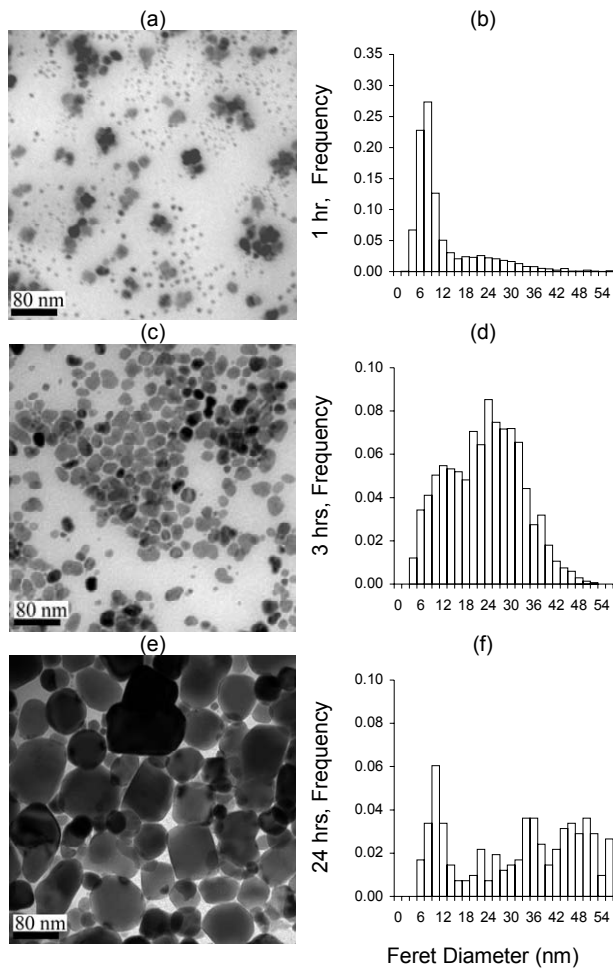
Fig. 4: Fe_3O_4 nanoparticles synthesized in the TOA-only system: (a-b) TEM image and PSD after 1 hour; (c-d) TEM image and PSD after 3 hours; (e-f) TEM image and PSD after 24 hours. Note that in (f) the distribution was truncated at 54 nm. However, the PSD continues with a maximum particle diameter near 104 nm [5].

Fig. 5: Fe_3O_4 nanoparticles synthesized in the HA/TOA system: (a-b) TEM image and PSD after 1 hour; (c-d) TEM image and PSD after 3 hours; (e-f) TEM image and PSD after 24 hours [5].

confirmed by the magnified TEM image in Fig. 7 of a single Fe_3O_4 nanoparticle grown in the HA/TOA system, where the lattice fringes are resolved confirming the single crystal nature of the particle. As shown by the tilt series and PSD evolution, the greater affinity of HA to the surface of the iron oxide appears not only to slow the growth of the particles, but also improve the nanoparticle crystal structure, preventing the formation of polycrystalline domains in the particles. The slower observed growth rates could be due to the inhibition of monomer incorporation, inhibition of coarsening mechanisms, or a combination of both [32]. The HA/TOA particles are in general single crystals; however, twinning defects are present in some of the particles as seen in particles 'd' and 'e' of the 0° HA/TOA tilt frame. Similar to previous observations of highly crystalline biogenic magnetite, twin defects are seen in TEM images as a light line dissecting the particle into halves [34].

The PSD of the particle sizes for the TOA-only system display a distinctly bimodal distribution at 3 hours (Fig. 4d). The early development of the second peak is also seen in the 1 hour al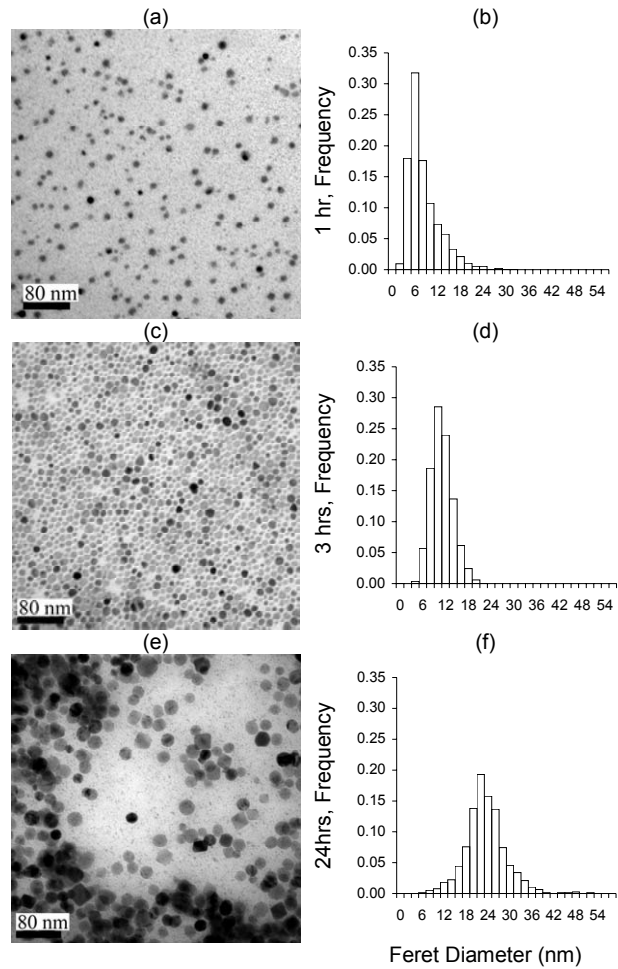iquot. It is worth noting that bimodal distributions have been observed in micelle-mediated particle syntheses under conditions where the micelle film flexibility and reagent concentration meet specific criteria [35, 36]. Monte Carlo simulations of these micelle systems attribute the bimodality of the PSD to the operation of multiple coarsening mechanisms in the equilibration process (i.e., coalescence and Ostwald ripening) [36]. While the parallels between micelle-based reactions and our solvo-thermal process are limited, it may be worth exploring in future studies the relationship between monomer concentration, capping agent affinity and the existence of bimodal PSD's in solvo-thermal reactions.

Given the irregular shape and polycrystalline nature of the particles synthesized in TOA alone (Fig. 6, upper panel), there is evidence to indicate that Smoluchoski ripening is more prevalent in this system (especially at times <24 hrs). These polycrystals can be thought of as individual crystallites that have been incorporated into a larger particle through coalescence. Since the time scale for the coalescence is short due to mixing, there is no time for the incorporated crystals to undergo restructuring to a more energetically favorable single crystal structure. As a consequence, the particles exhibit irregular shapes and polycrystalline structure at short and
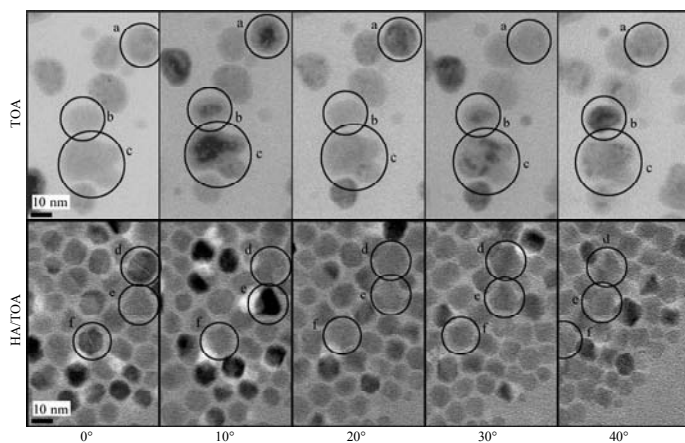
Fig. 6: HRTEM tilt series taken at 0°, 10°, 20°, 30° and 40°. The upper row shows the TOA-only aliquot, while the lower row shows the HA/TOA aliquot series. Both aliquots were taken after a 3 hour reaction period. The labeled circles follow selected particles through the tilt series. HA/TOA particles 'd' and 'f' show evidence of twin defects at 0° tilt [5].
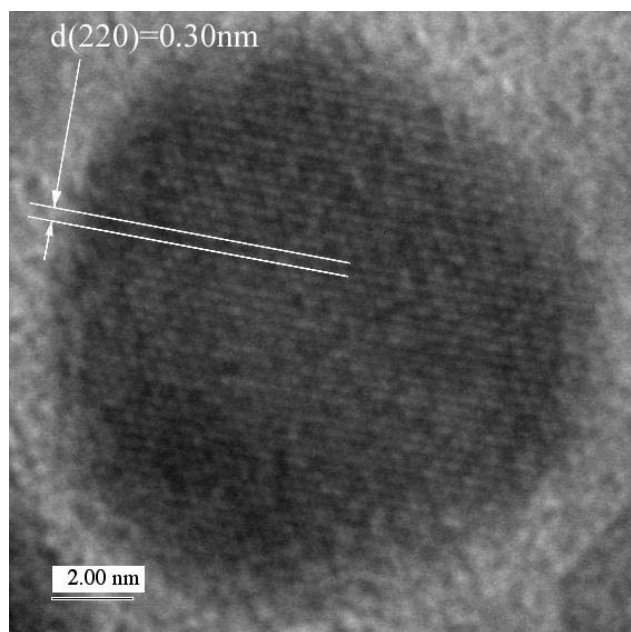

Fig. 7: Lattice fringes showing the single crystal nature of the magnetite synthesized in HA/TOA at 3 hours. The indicated lattice spacing is concurrent with magnetite's (220) plane [5].

intermediate times (Fig. 4 a and c). As reaction times approach 24 hours, the large population of smaller particles has previously coalesced, thus forming a smaller number of large polycrystalline particles that continue to ripen with time. In this scenario, Smoluchowski ripening gives way to Ostwald ripening as the dominant coarsening mechanism [27]. This is validated by our observation at later times that restructuring via Ostwald ripening yields faceted crystalline structures with smooth edges (Fig. 4e), hence a more energetically favorable atomic configuration. XRD broadening and TEM image analyses confirm that the TOA-only system at 24 hours is primarily composed of large single crystal particles.

While the TOA-only system is crystalline at 24 hours as indicated by faceting in the TEM images, the PSD indicates a highly polydisperse ensemble (Fig. 4e-f). This agrees with the general trend of increasing polydispersity with time as seen in the PSD's measured at 1 and 3 hours. In contrast, the PSD's for the HA/TOA system shown in Fig. 5 yield standard deviations of 54%, 28%, and 25% at 1, 3, and 24 hours, respectively. This trend indicates a focusing effect similar to that observed in diffusion-based growth processes [37, 38]. As mentioned previously, the addition of HA slows nanoparticle growth and maintains a relatively narrow PSD when compared to the ever widening PSD of the TOA-only system. It should be noted that at 72 hours, the HA/TOA PSD deviates from the earlier trend, and becomes highly polydisperse (not shown). This trend is previously observed by other researchers [27], and possibly indicates either a boiling off or degradation of the HA stabilizing agent (BP=260°C) after prolonged reaction times.

The addition of a high-affinity stabilizing agent such as HA is shown to slow overall growth rates and prevent unwanted particle coalescence. Without the addition of HA, the TOA-only reaction displays rapid, unrestrained coalescence at early times yielding an intermediate growth stage composed of irregular, polycrystalline particles. Late stage growth in the TOA-only system is dominated by Ostwald ripening and atomic restructuring processes, which act to smooth the particle edges and remove grain boundaries through diffusion processes (Fig. 4e). Therefore, we can conclude that the Lewis acid strength of the solvent, and the addition of a high-affinity stabilizing agent, can significantly impact the resulting crystal structure and size distribution of the resulting nanoparticle ensemble. Also critical to any nanoparticle synthesis protocol is the resulting material properties of the ensemble, such as the magnetic behavior. To this end, we have performed a comprehensive characterization of the magnetic properties of the nanoparticles synthesized in the HA/TOA and TOA-only systems. With these results, we can link the observed changes in crystal structure and size distribution to the measured magnetic properties for nanoparticles grown from differing solution chemistries.

To compare the magnetic properties resulting from the HA/TOA and TOA-only synthetic protocols, we examined nanoparticles obtained after a synthesis time of 3 hours, which yielded particles measuring 10 nm and 24 nm in diameter, respectively (Fig. 5c-d and Fig. 4c-d). These samples were chosen for their relatively narrow PSD as determined over the duration of each experimental run and the differences in crystal structure observed by TEM and XRD. When considering the effects of surface spin disorders, ligand-oxide surface bonding interactions, and the finite size effect in single crystals [22, 39], the 24 nm particles would normally be expected to display a larger magnetization (M) and saturation magnetization (M_s) than the 10 nm particles. To explore this, the M_s was obtained for each size at room temperature (300 K, Fig. 8) using a high-field fit to the expression $M = M_s(1 - A/H^2)$, where A is a field independent parameter and H is the applied field. Using this relationship to calculate M_s at infinite field, the 10 nm particles measured 51 A·m^2/kg at 300 K (bulk magnetite = 87 A·m^2/kg). The 24 nm particles gave an M_s of 49 A·m^2/kg at 300K. According to these calculated values from the field sweep curves, the M_s for the 10nm particles was similar to the 24 nm ensemble. In addition, the zero field cooled (ZFC) and field
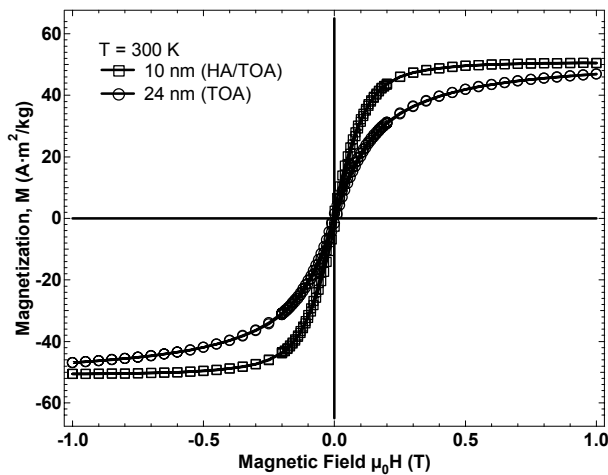
Fig. 8: Magnetization as a function of applied field measured at 300 K. The 10 nm particles (□) were synthesized in the presence of TOA and HA, while the 24 nm particles (○) were synthesized in the presence of TOA-only [5].
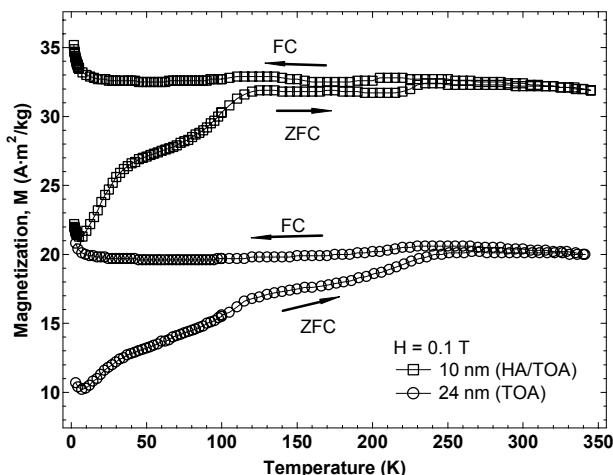

Fig. 9: Field cooled (FC) and zero field cooled (ZFC) magnetization for 10 nm (HA/TOA, □), and 24 nm (TOA, ○) particles [5]. The change in the slope on the ZFC graph indicates the Verway transition occurring over the temperature range of 100-120 K [39].

cooled (FC) plots shown in Fig. 9 give a much higher magnetization for the 10nm particles when compared to the 24 nm particles. This is contrary to what would be expected if both systems contained particles made up of single crystals, especially when considering the negative effects of surface spin disorders in smaller particles due to high surface-to-volume ratios. However, unlike the 10 nm single crystals obtained with the HA/TOA system, our TEM and XRD data indicate that the 24 nm particles made in the TOA-only system are actually polycrystalline with an average crystallite size of 10 nm (Fig. 3a). Therefore, the polycrystalline nature of the 24 nm particles negatively affects the magnetic anisotropy, K, due to the increased number of grain boundaries present in each particle. Furthermore, the more polydisperse nature of the TOA-only sample may also result in the decreased M and M_s values. Therefore, we believe that the larger M and M_s values obtained are due to the single crystal, less polydisperse nature of the nanoparticles grown with a high-affinity stabilizing agent [5].

To validate the unexpected values of M and M_s as a function of size, the anisotropy constant, K, was calculated
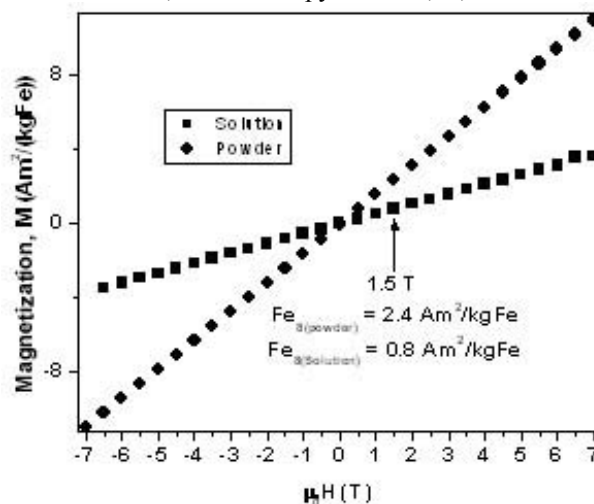

Fig. 10: Comparison of the DC magnetization of Fe_8 powder as dissolved in DI H_2O at room temperature [6].

using the relation for superparamagnetic particles, $T_B = KV/25k$, where T_B is the blocking temperature, k is the Boltzmann constant, and V is the particle volume. From Fig. 9, T_B is estimated to be 240 K and 270 K for the 10 nm and 24 nm particles, respectively. Therefore, the anisotropy constant for the 10 nm and 24 nm magnetic nanoparticles is 15.8 x 10^4 J/m^3 and 1.29 x 10^4 J/m^3, respectively. The reduced anisotropy value for the larger 24 nm particles validates our counterintuitive magnetization results and is supported by the polycrystalline nature of these particles as observed by TEM.

Field sweep SQUID measurements of Fe_8 are shown in Fig. 10 [6]. As expected, the contribution of the highly concentrated unpaired electrons in the Fe_3O_4 nanoparticles results in a significantly higher magnetization (Fig. 8) than the Fe_8 (Fig. 10) at low field strengths. However, as can be seen in the Fe_8 field sweep, the magnetization does not saturate, and appears to be linearly dependant over the range of -7 to 7 Tesla. The MION preparation in this paper saturated below 1 Tesla, while the magnetization of the Fe_8 superparafluid and powder continues to increase with field. This indicates a potential gain in contrast relative to conventional preparation as MRI proceeds to higher fields.

As shown in Fig. 8 and Fig. 10, the lack of hysteresis in the field sweep graphs indicates that the Fe_3O_4 nanoparticles and Fe_8 molecules are superparamagnetic. Thus, we expect these contrast agents to display negative contrast improvement when a T_2 weighted MR imaging sequence is used. In Fig. 11 we see the result of T_1 and T_2 weighted imaging sequences performed on three samples: a DI H_2O control, a 1.9 μM solution of the 10 nm Fe_3O_4 nanoparticles in DI H_2O, and a 1.9 μM solution of the 24 nm Fe_3O_4 nanoparticles in DI H_2O. As expected, the highly crystalline (thus, high magnetic moment) 10 nm nanoparticles provide the greatest T_2 negative contrast. While the 24 nm particles are present in the same concentration, the resulting T_2 negative contrast is better than the DI H_2O control, but produce less T_2 shortening of the hydrogen protons. These results agree with our analysis of the SQUID data in Fig. 8 and Fig. 9 in which the higher magnetization of the 10 nm
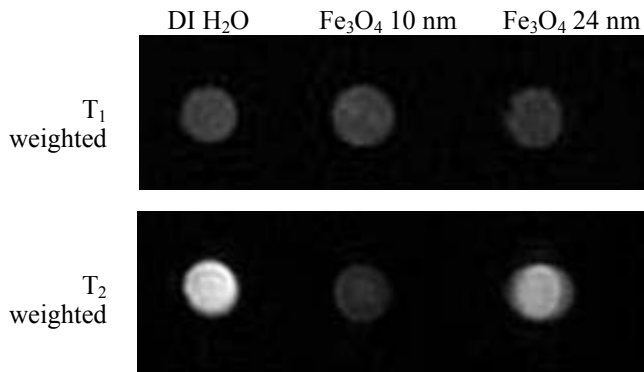
DI H$_2$O   Fe$_3$O$_4$ 10 nm   Fe$_3$O$_4$ 24 nm

T$_1$
weighted

T$_2$
weighted

Fig. 11: T$_1$ and T$_2$ weighted MRI phantoms of the Fe$_3$O$_4$ nanoparticle ensembles dispersed in DI H$_2$O. Note the 10nm particles have the most negative contrast. Phantoms in the left column are DI H$_2$O controls.
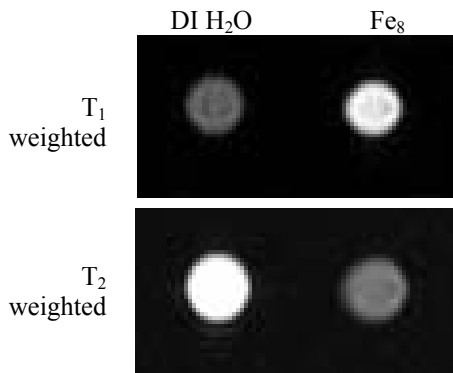

DI H$_2$O   Fe$_8$

T$_1$
weighted

T$_2$
weighted

Fig. 12: T$_1$ and T$_2$ weighted MRI phantoms of the Fe$_8$ solution dispersed in DI H$_2$O. Note that the Fe$_8$ solution both provides a positive contrast and negative contrast for T$_1$ and T$_2$ weighted sequences, respectively. Phantoms in the left column are DI H$_2$O controls [6].

nanoparticles would have a larger effect on adjacent proton T$_2$ relaxation times.

In Fig. 12, we see the result of T$_1$ and T$_2$ weighted imaging sequences performed on two samples: a DI H$_2$O control and a 0.0046 M solution of Fe$_8$ molecules in DI H$_2$O [6]. As expected from our field dependant magnetization measurements, a negative contrast occurs with the T$_2$ weighted sequence. It should be noted that the pulse sequence used for the Fe$_8$ are different from the Fe$_3$O$_4$ pulse sequences as mentioned in the Methods section (which was required to optimize the contrast for each type of molecular contrast agent). Keeping the different pulse sequences in mind, it is not surprising that the T$_2$ negative contrast of the Fe$_8$ appears to be less than that of the Fe$_3$O$_4$ 10 nm particles given the field dependant magnetization curves. At 1.0 T the magnetization of the powders differ by an order of magnitude, which would indicate that the T$_2$ shortening of the hydrogen protons surrounding a Fe$_8$ molecule would be less than those protons surrounding a Fe$_3$O$_4$ nanoparticle. Thus, we expect a reduction in the negative contrast improvement. However, the potential for Fe$_8$ to be used as an extravascular T$_2$ shortening agent outweighs the observed reduction in negative contrast effectiveness.

CONCLUSION

Fe$_3$O$_4$ nanoparticles are synthesized by solvo-thermal processing with and without an added stabilizing agent. From temporal PSD and XRD analyses, HRTEM tilt series experiments, and SQUID magnetometry, we demonstrate that the negative effects of coarsening mechanisms on crystal structure can be inhibited with the appropriate inclusion of one or more stabilizing agents. By including HA, a strong Lewis acid stabilizing agent, particle growth rates in the ripening phase are slowed thus yielding nanocrystalline particles at growth times as long as 24 hours. After growth for 3 hours, the PSD is observed to narrow indicating a focusing effect at intermediate times. For longer growth times, the PSD is observed to defocus yielding a broader size distribution of single crystalline magnetite particles. Without the inclusion of HA, growth rates are uncontrolled in the TOA-only system resulting in larger particles having a broad PSD even at short growth times (1 hour) and interfacial defects such as grain boundaries. With the inclusion of a stabilizing agent such as HA, the resultant single crystal particles grown for 3 hours possess a higher magnetic anisotropy than particles grown in the TOA-only system. The reduced magnetic anisotropy value for the TOA-only system is attributed to the polycrystalline nature of the nanoparticles. By SQUID magnetometry we also observe that the saturation of our tailored Fe$_3$O$_4$ occurs below 1 Tesla, while the Fe$_8$ powder and superparafluid remain linearly dependent beyond 7 Tesla, which could prove useful as clinical diagnostic imaging moves to higher field strengths. According to the MRI T$_2$ weighted images, tailored Fe$_3$O$_4$ nanocrystals and Fe$_8$ SMMs show promise for T$_1$ and T$_2$ weighted contrast imaging.

REFERENCES

[1] Wickline, S. A. and Lanza, G. M., 2002, "Molecular Imaging, Targeted Therapeutics, and Nanoscience," Journal of Cellular Biochemistry, Vol., pp. 90-97.

[2] Flacke, S., Fischer, S., Scott, M. J., Fuhrhop, R. J., Allen, J. S., McLean, M., Winter, P., Sicard, G. A., Gaffney, P. J., Wickline, S. A. and Lanza, G. M., 2001, "Novel MRI Contrast Agent for Molecular Imaging of Fibrin Implications for Detecting Vulnerable Plaques," Circulation, Vol. **104**, pp. 1280-1285.

[3] Ruehm, S. G., Corot, C., Vogt, P., Kolb, S. and Debatin, J. F., 2001, "Magnetic resonance imaging of atherosclerotic plaque with ultrasmall superparamagnetic particles of iron oxide in hyperlipidemic rabbits," Circulation, Vol. **103**, pp. 415-422.

[4] Lanza, G. M., Yu, X., Winter, P. M., Abendschein, D. R., Karukstis, K. K., Scott, M. J., Chinen, L. K., Fuhrhop, R. W., Scherrer, D. E. and Wickline, S. A., 2002, "Targeted

Antiproliferative Drug Delivery to Vascular Smooth Muscle Cells with a Magnetic Resonance Imaging Nanoparticle Contrast Agent Implications for Rational Therapy of Restenosis," Circulation, Vol. **106**, pp. 2842-2847.

[5] Barker, A. J., Cage, B., Russek, S. and Stoldt, C., 2005, "Ripening during Magnetite Nanoparticle Synthesis: Resulting Interfacial Defects and Magnetic Properties," Journal of Applied Physics, Submitted.

[6] Cage, B., Barker, A., Russek, S., Stoldt, C., Lanning, C., Garg, R., Shandas, R., Zipse, D. and Dalal, N., 2005, "Single-molecule magnets hold promise as water-soluble iron-based magnetic resonance imaging contrast agents of a size less than 5 nm," NMR in Biomedicine, Submitted.

[7] Callister, W. D., *Materials Science and Engineering: An Introduction*. 4th ed. 1997, New York: John Wiley & Sons, Inc.

[8] Bjornerud, A. and Johansson, L., 2004, "The Utility of Superparamagnetic Contrast Agents in MRI: Theoretical Consideration and Applications in the Cardiovascular System," NMR in Biomedicine, Vol. **17**, pp. 465-477.

[9] Miles, P. A., Westphal, W. B. and von Hippel, A., 1957, "Dielectric Spectroscopy of Ferromagnetic Semiconductors," Review of Modern Physics, Vol. **29**, pp. 279-307.

[10] Lembke, U., Hoell, A., Kranold, R., Muller, R., Schuppel, W., Goerigk, G., Gilles, R. and Wiedenmann, A., 1999, "Formation of Magnetic Nanocrystals in a Glass Ceramic Studied by Small-Angle Scattering," Journal of Applied Physics, Vol. **85**, pp. 2279-2286.

[11] Delfs, C., Gatteschi, D., Pardi, L., Sessoli, R., Wieghardt, K. and Hanke, D., 1993, "Magnetic-Properties of an Octanuclear Iron(III) Cation," Inorganic Chemistry, Vol. **32**, pp. 3099-3103.

[12] Gatteschi, D. and Sessoli, R., 2003, "Quantum Tunneling of Magnetization and Related Phenomena in Molecular Materials," Angewandte Chemie-International Edition, Vol. **42**, pp. 268-297.

[13] Hobbs, S. K., 1998, "Regulation of Transport Pathways in Tumor Vessels: Role of Tumor Type and Microenvironment," in Proceedings of the National Academy of Sciences, USA, Vol. 95, pp. 4607-4612.

[14] Zipse, D., North, J. M., Dalal, N. S., Hill, S. and Edwards, R. S., 2003, "Characterization of the S=9 excited state in Fe8Br8 by electron paramagnetic resonance," Physical Review B, Vol. **68**, pp. -.

[15] Park, K., Novotny, M. A., Dalal, N. S., Hill, S. and Rikvold, P. A., 2002, "Effects of D-strain, g-strain, and dipolar interactions on EPR linewidths of the molecular magnets Fe-8 and Mn-12," Physical Review B, Vol. **65**, pp. -.

[16] Murray, C. B., Kagan, C. R. and Bawendi, M. G., 2000, "Synthesis and Characterization of Monodisperse Nanocrystals and Close-Packed Nanocrystal Assemblies," Annual Review of Materials Science, Vol. **30**, pp. 545-610.

[17] Sun, S. H. and Murray, C. B., 1999, "Synthesis of Monodisperse Cobalt Nanocrystals and Their Assembly into Magnetic Superlattices (invited)," Journal of Applied Physics, Vol. **85**, pp. 4325-4330.

[18] Lin, X. M., Sorensen, C. M., Klabunde, K. J. and Hajipanayis, G. C., 1999, "Control of Cobalt Nanoparticle Size by the Germ-Growth Method in Inverse Micelle System: Size-Dependent Magnetic Properties," Journal of Materials Research, Vol. **14**, pp. 1542-1547.

[19] Zhang, D. J., Klabunde, K. J., Sorensen, C. M. and Hadjipanayis, G. C., 1998, "Magnetization Temperature Dependence in Iron Nanoparticles," Physical Review B, Vol. **58**, pp. 14167-14170.

[20] Leslie-Pelecky, D. L. and Rieke, R. D., 1996, "Magnetic properties of nanostructured materials," Chemistry of Materials, Vol. **8**, pp. 1770-1783.

[21] Fabian, K., Kirchner, A., Williams, W., Heider, F., Leibl, T. and Hubert, A., 1996, "Three-Dimensional Micromagnetic Calculations for Magnetite Using FFT," Geophysical Journal International, Vol. **124**, pp. 89-104.

[22] Hou, Y. L., Yu, J. F. and Gao, S., 2003, "Solvothermal Reduction Synthesis and Characterization of Superparamagnetic Magnetite Nanoparticles," Journal of Materials Chemistry, Vol. **13**, pp. 1983-1987.

[23] Hyeon, T., Lee, S. S., Park, J., Chung, Y. and Bin Na, H., 2001, "Synthesis of Hhighly Crystalline and Monodisperse Maghemite Nanocrystallites without a Size-Selection Process," Journal of the American Chemical Society, Vol. **123**, pp. 12798-12801.

[24] Sun, S. H. and Zeng, H., 2002, "Size-Controlled Synthesis of Magnetite Nanoparticles," Journal of the American Chemical Society, Vol. **124**, pp. 8204-8205.

[25] Peng, X. G., Manna, L., Yang, W. D., Wickham, J., Scher, E., Kadavanich, A. and Alivisatos, A. P., 2000, "Shape Control of CdSe Nanocrystals," Nature, Vol. **404**, pp. 59-61.

[26] Huang, F., Zhang, H. Z. and Banfield, J. F., 2003, "The Role of Oriented Attachment Crystal Growth in Hydrothermal Coarsening of Nanocrystalline ZnS," Journal of Physical Chemistry B, Vol. **107**, pp. 10470-10475.

[27] Huang, F., Zhang, H. Z. and Banfield, J. F., 2003, "Two-Stage Crystal-Growth Kinetics Observed During Hydrothermal Coarsening of Nanocrystalline ZnS," Nano Letters, Vol. **3**, pp. 373-378.

[28] Lu, K., 1996, "Nanocrystalline metals crystallized from amorphous solids: Nanocrystallization, structure, and properties," Materials Science & Engineering R-Reports, Vol. **16**, pp. 161-221.

[29] Thomas-Keprta, K. L., Bazylinski, D. A., Kirschvink, J. L., Clemett, S. J., McKay, D. S., Wentworth, S. J., Vali, H., Gibson, E. K. and Romanek, C. S., 2000, "Elongated prismatic magnetite crystals in ALH84001 carbonate globules: Potential Martian magnetofossils," Geochimica Et Cosmochimica Acta, Vol. **64**, pp. 4049-4081.

[30] Johansson, E. and Nyborg, L., 2000, "XPS study of surface-active organic compounds on fine ferrous powder," Surface and Interface Analysis, Vol. **30**, pp. 333-336.

[31] Johansson, E. and Nyborg, L., 2003, "XPS study of carboxylic acid layers on oxidized metals with reference to particulate materials," Surface and Interface Analysis, Vol. **35**, pp. 375-381.

[32] Murray, C. B., Sun, S. H., Gaschler, W., Doyle, H., Betley, T. A. and Kagan, C. R., 2001, "Colloidal Synthesis of Nanocrystals and Nanocrystal Superlattices," IBM Journal of Research and Development, Vol. **45**, pp. 47-56.

[33] Shevchenko, E. V., Talapin, D. V., Schnablegger, H., Kornowski, A., Festin, O., Svedlindh, P., Haase, M. and

Weller, H., 2003, "Study of Nucleation and Growth in the Organometallic Synthesis of Magnetic Alloy Nanocrystals: The Role of Nucleation Rate in Size Control of CoPt3 Nanocrystals," Journal of the American Chemical Society, Vol. **125**, pp. 9090-9101.

[34] Devouard, B., Posfai, M., Hua, X., Bazylinski, D. A., Frankel, R. B. and Buseck, P. R., 1998, "Magnetite from Magnetotactic Bacteria: Size Distributions and Twinning," American Mineralogist, Vol. **83**, pp. 1387-1398.

[35] Tojo, C., Blanco, M. C. and LopezQuintela, M. A., 1997, "Preparation of nanoparticles in microemulsions: A Monte Carlo study of the influence of the synthesis variables," Langmuir, Vol. **13**, pp. 4527-4534.

[36] Tojo, C., Blanco, M. C. and Lopez-Quintela, M. A., 1998, "The Influence of Reactant Excess and Film Flexibility on the Mechanism of Nanoparticle Formation in Microemulsions: A Monte Carlo Simulation," Langmuir, Vol. **14**, pp. 6835-6839.

[37] Sugimoto, T., 1987, "Preparation of Monodispersed Colloidal Particles," Advances in Colloid and Interface Science, Vol. **28**, pp. 65-108.

[38] Peng, X. G., Wickham, J. and Alivisatos, A. P., 1998, "Kinetics of II-VI and III-V Colloidal Semiconductor Nanocrystal Growth: "Focusing" of Size Distributions," Journal of the American Chemical Society, Vol. **120**, pp. 5343-5344.

[39] Goya, G. F., Berquo, T. S., Fonseca, F. C. and Morales, M. P., 2003, "Static and Dynamic Magnetic Properties of Spherical Magnetite Nanoparticles," Journal of Applied Physics, Vol. **94**, pp. 3520-3528.